PLANT SCIENCE TODAY
Vol 13(sp4): 1-18
https://doi.org/10.14719/pst.12861

eISSN 2348-1900

RESEARCH ARTICLE

Pharmacognostic and bioefficacy analysis of crude extracts and biosynthesised nanoparticles from *Chenopodium murale* L.

Divya Kumari[1], Megha Sharma[1], Priyesh Sharma[1], Priya Chaudhary[2], Anand Prakash[1] & Pracheta Janmeda[1]*

[1]Department of Bioscience and Biotechnology, Banasthali Vidyapith, Banasthali 304 022, Rajasthan, India
[2]Centre for Herbal Pharmacology and Environmental Sustainability, Chettinad Hospital and Research Institute, Chettinad Academyof Research and Education, Kelambakkam, Chennai 603 103, Tamil Nadu, India

*Correspondence email - pracheta@banasthali.in

Received: 22 November 2025; Accepted: 30 April 2026; Available online: Version 1.0: 19 June 2026

Cite this article: Divya K, Megha S, Priyesh S, Priya C, Anand P, Pracheta J. Pharmacognostic and bioefficacy analysis of crude extracts and biosynthesised nanoparticles from *Chenopodium murale* L. Plant Science Today. 2026; 13(sp4): 1-18. https://doi.org/10.14719/pst.12861

Abstract

The present study investigates the pharmacognostic characteristics, physicochemical parameters, antioxidant potential, antimicrobial activity and plant-based synthesis of zinc oxide nanoparicles (Zn-O-NPs) and iron oxide nanoparticles (Fe-O-NPs) using sequential Soxhlet extracts of *Chenopodium murale* L. Microscopic fluorescence analysis exhibited distinct colour emissions under UV light, supporting the authentication and purity of the plant material. Physicochemical evaluation revealed total ash (26.05 % in stem), acid-insoluble ash (21.62 % in roots) and moisture content (75.62 % in leaves) within World Health Organization (WHO) recommended limits, indicating acceptable quality standards. Phytochemical screening demonstrated the presence of alkaloids, flavonoids, phenolics, glycosides and tannins, with higher abundance in the ethanolic leaf extract. The plant-based synthesis of Zn-O-NPs and Fe-O-NPs showed characteristic UV–Visible absorption peaks at 353 nm and 311 nm, respectively. Particle size analysis indicated average diameters of 190 nm for Zn-O-NPs and 189 nm for Fe-O-NPs, while FE-SEM and TEM analyses confirmed predominantly spherical morphology. The *in vitro* antioxidant assays revealed that the ethanolic leaf extract exhibited notable metal chelating ability, ferric reducing power and DPPH free radical scavenging activity, achieving 76.28 %, 73.84 % and 67.08 % inhibition at 1.0 mg/mL, respectively. Furthermore, the biosynthesized nanoparticles demonstrated significant antimicrobial and antifungal efficacy, producing maximum inhibition zones of 34 mm and 36 mm, respectively, surpassing the activity of crude extracts. Overall, the findings highlight *C. murale* as a promising natural source for eco-friendly nanoparticle synthesis and a potential candidate for developing therapeutic agents against oxidative stress and microbial infections.

Keywords: antimicrobial; antioxidant activity; *Chenopodium murale*; disc diffusion; green synthesis; iron oxide nanoparticles; metal chelataion; pharmacognosy; physicochemistry; zinc oxide nanoparticles

Introduction

The use of medicinal plants as medicinal purpose is not new to prehistoric period. The growing popularity of herbal medicines in the world has mainly been associated with the escalation of drug resistance, adverse effects of synthetic drugs and high cost of treatment. Phytochemicals that regulate enzymes are defined and have emerged as the best targets of treatment. It is usually believed that phytochemicals in a plant have a benefit by eliminating toxic oxidative stress or products, lipid oxidation inhibition and reducing rancidity (1).

Chenopodium murale L. (family- Amaranthaceae; order- Caryophylales) is an underexploited species with a huge pharmacological potential. It is an annual herb that is commonly referred to as nettle-leaved goose foot or sowbane and is commonly found in tropical and temperate areas. Besides being a weed the members of the respective family was seen to be medically active as diaphoretic, stomachic, amenorrhea analgesic, anthelmintic, antispasmodic, migraine, depression, antihypertensive and asthma relief (2). Thus, the research was conducted to compare pharmacognostic and antioxidant characteristics of various parts (roots, stems and leaves) of *C. murale*.

The new development in nanobiotechnology has given new dimension to the study of medicinal plants as it is now possible to biosynthesise metal oxide nanoparticles through environmentally friendly procedures. The nanoparticle biosynthesis by use of plant extracts provides a promising alternative to the traditional chemical and physical processes, which avoid the employment of toxic reagents and improves biocompatibility. Phytochemicals in plant extracts are reducing agents and stabilising agents that allow the production of nanoparticles with a defined morphology and active functional behaviour. Two of the most common nanoparticles are zinc oxide (Zn-O-NPs) and iron oxide nanoparticles (Fe-O-NPs), which have been identified to have their own unique optical, antimicrobial and antioxidant properties and are potential in biomedical, environmental and pharmaceutical uses (3).

Nevertheless, no study has so far reported the simultaneous production of Zn-O and Fe-O-NPs by *C. murale* as well as the pharmacognostic and phytochemical experiment of the product. This has a two-fold benefits of verifying the medicinal authenticity of the plant and exploiting the phytoconstituents of the plant to develop sustainable nanomaterials. The present study conducted to do: (i) the pharmacognostic and phytochemical characterisation

of *C. murale* to determine quality control parameters; (ii) biosynthesise and characterise the Zn-O and Fe-O-NPs with their ethanolic extracts; and (iii) determine the antioxidant and antimicrobial activities of both crude extracts and the biosynthesised nanoparticles.

The synthesised Zn-O-NPs and Fe-O-NPs from *C. murale* demonstrated promising *in vitro* antioxidant and antimicrobial activities, indicating their potential for biomedical and environmental applications. However, these findings are preliminary and further *in vivo* studies and detailed safety assessments are required to validate their practical applicability. Therefore, the present results should be considered as an initial step toward exploring their broader therapeutic and environmental potential as well as interconnects the ancient ethnomedicinal data to the current nanotechnology.

Materials and Methods

Chemicals and solvents utilised

All chemicals, reagents and solvents used in the study were of analytical grade and procured from HiMedia Laboratories (Maharashtra, India) and Sigma-Aldrich (Burlington, MA, USA).

Validation of plant

The experimental plant was collected (October, 2018), identified (Altitude- 26°24′14.8414″ and Latitude- 73°52′9.7194″) and authenticated by the 'Krishi Vigyan Kendra', Banasthali Vidyapith, Rajasthan (304022) with species plantarum number: Sp. Pl. 1: 219 (1753).

Preparation of extracts

The collected plant materials were washed with distilled water, shade-dried and pulverised into fine powder. Sequential extraction was performed using solvents of increasing polarity in a Soxhlet apparatus, followed by concentration under reduced pressure using a rotary evaporator and storage at 4 °C until further analysis. The percentage extraction yield (w/w %) was calculated using a standard formula as described below (4, 5):

$$\text{Extraction yield (\%)} = \frac{\text{Weight of plant extract (sample)}}{\text{Weight of dried plant extract (powder)}} \times 100$$

Physicochemical analysis

Physicochemical studies, such as finding the total ash, moisture content, water-soluble ash, acid-insoluble ash and pH (1 and 10 % solutions) were conducted to ascertain adequacy of standardisation and authentication of the plant material. The purity and quality of the crude drug and the potential presence of impurities or adulterants was determined using fresh powdered samples. Every action was done according to the World Health Organization (WHO) guidelines (6).

Pharmacognostic (fluorescence) assay

Test tubes with the finely powdered samples prepared of the different parts of the plant were treated with certain reagents and chemicals. The fluorescence properties were investigated using a fluorescence microscope following a period of a couple of min (Leica DM 100) of the mixture under both visible light and at the ultraviolet wavelengths i.e. short UV (254 nm) and long UV (366 nm) (7).

Phytochemical analysis

Phytochemical analysis assists in the determination of presence and non-presence of various primary and secondary plant metabolites. This study relies on the observable reactions, which include color development, precipitates formation, or other observable reactions. The extracts obtained from various parts (leaves, stems and roots) of *C. murale* were analysed to determine the different metabolites such as amino acids, carbohydrates, flavonoids and tannins, etc (8).

Nanoparticles synthesis

Zinc oxide nanoparticles

The plant extract and metal salt solution were mixed in a fixed ratio of [1:9, v/v], using a precursor (zinc acetate dihydrate) concentration of [e.g., 0.1 M]. The two mixtures were stirred and left to heat at 60 °C and temperature. The pH was recorded again (pH: ~8.0–9.0) after this time to determine the reaction was complete and the formation of the nanoparticles. The mixture that resulted was centrifuged at 10000 rpm (11180 × g, using a rotor with a radius of 10 cm) with 40 °C temperature and allowed to centrifuge over a period of 20 min. The resulting pellets of Zn-O-NPs were twice washed in the deionised water at the same centrifugation rate. The pellets were then washed and dried in an oven at 100 °C. They were dried and then finely ground in a mortar and pestle. The powdered samples were then annealed in a furnace with temperatures of 400 °C over the course of 2 hr in order to remove any impurities that may remain. All reactions were performed under (ambient atmosphere) conditions (9).

Iron oxide nanoparticles

The starting material of the synthesis of Fe-O-NPs was ferric chloride hexahydrate ($FeCl_3$-$6H_2O$). The extract of the plant was slowly dropped over a solution of ferric chloride in various molar ratios of 0.25 : 0.5 : 1 and 1 : 1 listed as 01 : 04, 02 : 04 and 01 : 01 respectively. The mixture was then kept on a magnetic stirrer at 800 rpm (at pH: ~10.0–11.0) to allow the formation of nanoparticles to occur. At the end of the reaction, the Fe-O-NPs were centrifuged at 8000 rpm over a period of 10 min and formed pellets where the nanoparticles had been separated. The pellets were then rinsed (23 times) with ethanol and distilled water to get rid of any impurities or unreacted products. Lastly, the purified Fe-O-NPs pellets were kept under refrigeration to maintain the stability and allow ability in future experiments (10).

Characterisation of Zn-O-NPs and Fe-O-NPs

Visual observation and UV-visible analysis: The initial indication of successful synthesis of Zn-O and Fe-O-NPs was the visible colour change in the reaction mixture. The conversion of zinc and iron ions into their respective nanoparticles through reduction by the plant extract was analysed using a UV–Visible doublebeam spectrophotometer (Systronics, Ahmedabad, Gujarat, India). The absorbance was recorded at room temperature within a wavelength range of 300 to 700 nm at various time intervals i.e., 10, 30 and 90 min and 24 hr. Solutions of 1 mM zinc acetate dihydrate and ferric chloride hexahydrate served as blanks for comparison.

X-ray diffraction analysis: X-Ray diffraction (XRD) analysis of the plant-mediated synthesised Zn-O-NPs and Fe-O-NPs was carried out using a Shimadzu XRD instrument (PXRD-7000). The diffraction patterns were recorded within a 2θ range of 30° to 80° employing CuKα radiation. The operating conditions included an energy of 8.04 keV, a wavelength of 1.54 Å, a voltage of 40 kV and a current of 25 mA. The crystallite size of the nanoparticles was determined

using Debye–Scherrer's equation as follows:

$D = (0.9 \times \lambda\lambda)/\beta\beta \times \text{Cos}\,\theta$

Where, D- crystal size (average); β- line broadening of radians; θ - Bragg's angle and λ- wavelength of X-ray.

Fourier transform-infrared analysis: Fourier transform-infrared (FT-IR) analysis (Bruker, Billerica, MA, USA) was used to study molecular vibrations, helping to determine the chemical groups responsible for the reduction, capping and stabilisation of the synthesised nanoparticles. The FT-IR spectra were recorded with a resolution of 2 cm^{-1} over a frequency range of 4000–400 cm^{-1}. For proper infrared measurement, pellets were prepared by mixing FT-IR grade potassium bromide (100 mg) with 1 mg of dried leaf powder, Zn-O-NPs, or Fe-O-NPs in a 1 : 100 ratio (11). The obtained spectra were then interpreted based on the characteristic infrared absorption frequencies corresponding to different functional groups.

Field emission scanning electron microscopy analysis: Field emission scanning electron microscopy (FE-SEM) (Tescan MIRA 3 LMU) was carried out following confirmation of nanoparticle formation through XRD analysis. The FE-SEM was used to examine the size, morphology, distribution and composition of the synthesized Zn-O-NPs and Fe-O-NPs. Prior to imaging, the samples were coated with a thin gold layer using a gold sputter coater. The coated slides were then placed in the Nano-SEM instrument for analysis.

Energy dispersive X-ray analysis: Elemental composition was determined using Energy dispersive X-ray (EDX) spectroscopy, which works by detecting X-rays emitted when electrons from higher energy levels fill vacancies in lower energy shells within the sample. The resulting X-ray energy, characteristic of each element, is measured by the EDX detector and represented as peaks in the generated spectrum.

Transmission electron microscopy analysis: Transmission electron microscopy (TEM) (JEM-F200 Multipurpose Electron Microscope) was further employed to study the detailed morphology, including shape and particle size, of Zn-O-NPs and Fe-O-NPs (12). Before TEM analysis, the samples were ultrasonicated for 1 hr using a probe sonicator. A clean iron grid was placed on Whatman filter paper and a small drop of the nanoparticle suspension was deposited slightly to one side of the grid to ensure even distribution. The prepared grids were then left to dry overnight before imaging.

Determination of antioxidant capacity

2,2-Diphenyl-1-picrylhydrazyl free radical scavenging activity

The 2,2-Diphenyl-1-picrylhydrazyl (DPPH) assay provides a measure of the extract's ability to neutralise free radicals, reflecting its antioxidant potential. Higher scavenging activity suggests that the plant extract can effectively counter oxidative stress, which is crucial for preventing cellular damage and associated diseases. The DPPH free radical scavenging activity of the plant extracts was evaluated with slight modifications to the standard method (13). Extracts were prepared in methanol at concentrations of 200–1000 µg/mL and 3 mL of each sample was mixed with 1 mL of 0.1 mM DPPH solution. After 30 min of incubation, absorbance was measured at 517 nm, with a decrease indicating higher radical scavenging activity. A blank containing 3 mL methanol and 1 mL DPPH solution was used and the percentage of DPPH inhibition was calculated.

$$\text{DPPH free radical scavenging activity (\%)} = \frac{(Ac - As)}{Ac} \times 100$$

Where, Ac- absorbance of ascorbic acid or AA (control) and As- absorbance in the presence of the extract.

Further, the inhibition concentration (IC50) was assessed by analysing the regression graph.

Ferric reducing antioxidant power

The antioxidant activity of the plant extracts was evaluated using the ferric reducing antioxidant power (FRAP) assay, which measures the reduction of ferric (Fe^{3+}) to ferrous (Fe^{2+}) ions in a redox-based colorimetric reaction. The FRAP assay reflects the electron-donating ability of the extracts, indicating their potential to act as reducing agents. A higher FRAP value signifies stronger antioxidant capacity, suggesting that the plant extract can effectively neutralise oxidative stress by converting reactive ferric ions into their stable ferrous form. Extract stock solutions were diluted to concentrations of 200–1000 µg/mL. The FRAP reagent was freshly prepared by mixing 10 mM TPTZ in 40 mM HCL, 20 mM $FeCl_3$ and 300 mM acetate buffer (pH 3.6) in a 1 : 1 : 10 ratio. Then, 1 mL of this reagent was added to each sample and incubated at room temperature for 30 min, after which absorbance was measured at 593 nm. The antioxidant activity, expressed as µM Fe (II)/g, was compared with the standard antioxidant butylated hydroxytoluene or BHT. A standard curve (y = mx + c) was used to determine the FRAP value of each extract (14).

$$C = c.\frac{V}{m}$$

Where, C- ferric reducing activity of plant extract in mg/g, c- concentration established from a standard curve (y), V- volume of extract (mL) and m- weight of plant extract (g).

Metal chelation activity

The ferrous ion chelating assay assesses the ability of plant extracts to bind and neutralise free iron ions, which catalyse oxidative reactions. A higher chelating capacity indicates stronger antioxidant potential, suggesting that the extracts may effectively prevent metal-induced oxidative damage in biological systems. The ferrous ion chelating activity of the plant extracts was evaluated using a modified method. A stock solution (1 mg/mL) was serially diluted to concentrations of 200–1000 µg/mL. Each reaction mixture contained 3.7 mL of methanol, 0.1 mL of 1 mM $FeCl_2$ and 0.2 mL of 5 mM ferrozine. After thorough mixing, the solutions were left to stand for 10 min at room temperature and absorbance was recorded at 562 nm against EDTA as a standard. A calibration curve (y = mx + c) was used to calculate the metal chelating potential of each extract (15).

$$\text{Metal chelation activity (\%)} = \frac{(Ac - As)}{Ac} \times 100$$

Where, Ac- absorbance of EDTA (control) and As- absorbance in the presence of the extract.

Antimicrobial activity of Zn-O-NPs and Fe-O-NPs

Disc-diffusion method: The antimicrobial activity of the synthesised Zn-O-NPs and Fe-O-NPs was evaluated using the disc diffusion method against *Bacillus subtilis* (Gram-positive), *Escherichia coli* and *Pseudomonas aeruginosa* (Gram-negative) and fungal strains *Aspergillus niger* and *Penicillium chrysogenum*. Microbial suspensions of 1.5×10^6 CFU/mL (bacteria) and 1.5×10^4

CFU/mL (fungi) were spread on MHA and PDA plates, respectively. Sterile 6 mm discs were loaded with 50 µL of nanoparticle samples, while gentamicin (10 µg), nystatin (2.5 µg) and ketoconazole (10 µg) served as positive controls. Plates were incubated at 35–37 °C for 24 hr (bacteria) and 72–120 hr (fungi). The inhibition zones were measured in millimetres using a vernier caliper. All experiments were performed aseptically in a Class II Biosafety Cabinet and repeated in triplicate.

Broth-dilution method: The minimum inhibitory concentration (MIC) of the synthesized Zn-O-NPs and Fe-O-NPswas determined using the broth dilution method in a 96-well microplate (100 µL/well). Test samples (8192 µg/mL) were serially diluted two-fold in MHB for bacteria and PDB for fungi, yielding concentrations from 4096 to 2 µg/mL. Microbial suspensions (1.5×10^6 CFU/mL for *B. subtilis*, *E. coli*, *P. aeruginosa*; and 1.5×10^4 CFU/mL for *A. niger* and *P. chrysogenum*) were added and incubated the bacteria at 35–37 °C for 24 hr and fungi at 25–28 °C for 72–120 hr. Ketoconazole or nystatin served as positive controls, while wells with inoculum only acted as negatives. Following incubation, 40 µL of resazurin dye (0.2 mg/mL) was added and re-incubated (30 min for bacteria; 1–1.5 hr for fungi). The MIC was noted as the lowest nanoparticle concentration maintaining the blue color of resazurin, indicating complete growth inhibition (16). Determining the MIC provides a quantitative measure of the antimicrobial potential of Zn-O-NPs and Fe-O-NPs biosynthesised from *C. murale*.

Statistical analysis

All experiments were conducted in triplicate and the data were represented as mean values accompanied by standard deviation (Mean ± SD). Antioxidant potentials of crude extracts and biosynthesised naoparticles were statistically compared using 'IBM SPSS Statistics version 20'. Graphical representations of the results were generated in 'Microsoft Excel 365'. Variations in the mean inhibition zones were regarded as statistically significant when $p < 0.05$ (ANOVA followed by post-hoc analysis). Additionally, the UV–Visible spectral data were processed and analysed using 'Origin Pro 8.5' software.

Results and Discussion

Extract preparation

Soxhlet extraction was used to extract different extracts of *C. murale* parts i.e., root, stem and leaves (Fig. 1). The filtrates were then extracted in a sequential manner the yield of filtrates was noted as 34.97 g/kg roots, 35.24 g/kg stems and 28.79 g/kg leaves. The extracts of the various parts of the plant were tested in terms of color, consistency and stability as described below in Table 1. Frequent physical analysis of the plant material is a necessary parameter in the development of a drug to determine potential adulteration and appropriate manipulation of the raw material (17). The different solvents that were used in the study leading to the variation in the yields of the extracts also showed that different phytochemical constituents were present in all the six solvent extracts of the plant under study.

Physicochemical analysis

Powdered samples of various locations of *C. murale* (roots, stems and leaves) were examined and the physicochemical properties were analysed as shown in Fig. 2. Adulteration may also occur as an accidental event and it can reduce the efficacies of the plants used in therapy and can be harmful in case they find their way into the food chain. Ash content is a useful method of identifying adulteration or contamination with inorganic matter, e.g. siliceous matter (insolubility of ash in water), or is used to determine the quality of crude drugs by reference to the water-soluble ash, which can be indicative of inappropriate processing or previous extraction with water.

The highest value of ash was detected in the stem (26.05 %), then the leaves (18.01 %) and roots (16.02 %), which means that it can be used to determine purity and quality of crude plant materials. The values of the highest acid-insoluble ash were observed in the roots (21.62 %), then in stems (21.30 %) and leaves

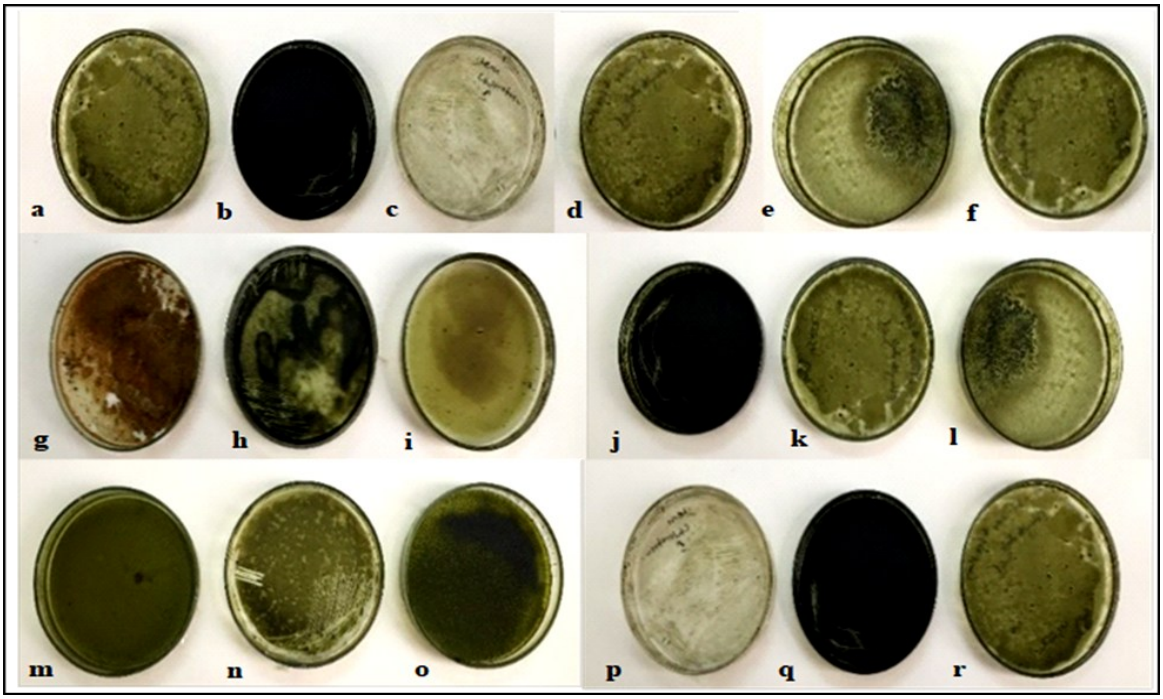


Fig. 1. Sequential extracts of different parts of *Chenopodium murale*. Root extracts: (a) petroleum ether, (b) benzene, (c) chloroform, (d) ethyl acetate, (e) methanol, (f) aqueous; stem extracts: (g) petroleum ether, (h) benzene, (i) chloroform, (j) ethyl acetate, (k) methanol, (l) aqueous; leaves extracts: (m) petroleum ether, (n) benzene, (o) chloroform, (p) ethyl acetate, (q) methanol and (r) aqueous.

Table 1. Preliminary phyto-profile (roots, stem and leaves) of *Chenopodium murale* in different solvents

Plant parts	Solvents	Boiling point (°C)	Polarity index	Consistency and color	Residue in g (Mean ± SD)	Weight of extract obtained in g (Mean ± SD)
Roots	Petroleum ether	60	0	Viscous, light green	38.04 ± 0.05	0.15 ± 0.009
	Benzene	80	2.7	Sticky, green	37.75 ± 0.04	0.14 ± 0.003
	Chloroform	61	4.1	Sticky, creamy	37.50 ± 0.06	0.15 ± 0.005
	Ethyl acetate	77	4.4	Powder, green	36.45 ± 0.03	0.22 ± 0.007
	Ethanol	78	5.2	Solid, black	36.23 ± 0.02	1.26 ± 0.002
	Water	100	9	Semi-solid, dark brown	34.97 ± 0.01	0.96 ± 0.001
Stems	Petroleum ether	60	0	Sticky, light green	49.58 ± 0.06	0.47 ± 0.002
	Benzene	80	2.7	Sticky, light green	47.83 ± 0.02	0.40 ± 0.003
	Chloroform	61	4.1	Sticky, brown	46.43 ± 0.03	0.30 ± 0.007
	Ethyl acetate	77	4.4	Powder, green	45.76 ± 0.04	0.41 ± 0.001
	Ethanol	78	5.2	Solid, black	39.90 ± 0.07	4.66 ± 0.009
	Water	100	9	Semi-solid, dark brown	35.24 ± 0.08	3.23 ± 0.02
Leaves	Petroleum ether	60	0	Sticky, light green	48.10 ± 0.09	0.91± 0.003
	Benzene	80	2.7	Sticky, green	46.34 ± 0.08	0.69 ± 0.002
	Chloroform	61	4.1	Sticky, light brown	45.82 ± 0.07	0.54 ± 0.01
	Ethyl acetate	77	4.4	Powder, green	43.81 ± 0.05	1.18 ± 0.001
	Ethanol	78	5.2	Solid, black	37.16 ± 0.004	5.11 ± 0.002
	Water	100	9	Semi-solid, dark brown	28.79 ± 0.05	5.67 ± 0.006

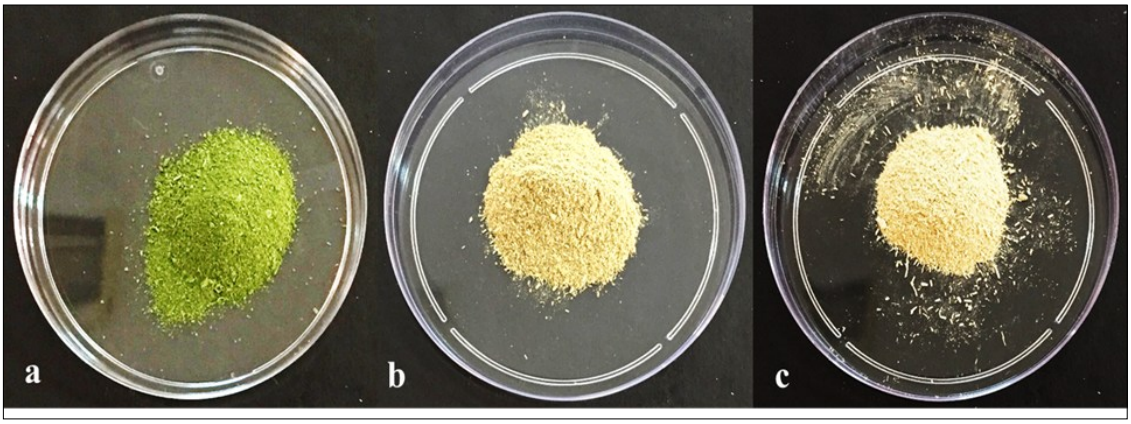


Fig. 2. Shade dried powdered form of different parts of *Chenopodium murale.* (a) Root; (b) stem; (c) leaves.

(12.06 %), indicating that there was the presence of siliceous impurities and environmental mineral content. In the meantime, the leaf contained the maximum percentage of water-soluble ash (76.34 %), then the stems (34.08 %) and roots (23.94 %), indicating the presence of acids, sugars and inorganic salts. According to WHO guidelines, total ash values for crude plant materials are generally expected to be ≤ 20 % (depending on plant species), acid-insoluble ash typically ≤ 5–10 % and moisture content should not exceed 8–14 % to ensure stability and prevent microbial contamination. In the present study, while total ash values for leaves and roots fall within acceptable limits, the comparatively higher values observed in stems and acid-insoluble fractions may be attributed to inherent mineral content or extraneous matter, which has been carefully considered during sample cleaning and processing.

The overall ash composition which is greater than the acid-insoluble ash is a significant value when determining the purity of plants since the latter is a measure of silica, carbonates and oxalates. The acid-insoluble values of the ash were relatively lower in the present study compared to water-soluble values, which means that there was minimal contamination (18). Nevertheless, the leaves had a relatively lower total ash value than the ash value that was insoluble in acid.

The high moisture level in plant materials encourages microbial activity, hydrolysis of the material by enzymes and degradation, whereas the low level of moisture supports increased stability and shelf life of the material and makes it more appropriate in drug development. One of the indicators of moisture, which is extremely important in terms of drying efficiency and product stability during storage, showed that the tested samples consisted of moisture exceeding the ideal, which is above the recommended moisture range (19). The loss-on-drying method showed that the leaves were the most wet (75.62 %) and the roots were the second-wettest (66.88 %) and the stems were the driest (46.02 %). The relatively high moisture content observed in the leaves (75.62 %) and roots (66.88 %) may be attributed to the natural water-retention capacity of parenchymatous tissues and the physiological characteristics of fresh plant material. According to WHO guidelines, elevated moisture levels can influence stability and may necessitate adequate post-harvest drying to ensure safe storage and prevent microbial deterioration; therefore, adequate post-harvest drying and controlled storage conditions are recommended to reduce moisture levels and ensure suitability for pharmaceutical formulation. The root of *C. murale* was found to have the highest pH of 8.4 ± 0.2 at 1 % and pH of 6.8 ± 0.4 at 10 %, possibly due to differential solubilisation of phytoconstituents at varying concentrations. All the results are summarised in Table 2.

Table 2. Physicochemical analysis of different parts (root, stem and leaves) of *Chenopodium murale*

Plant parts	Total ash content	Acid insoluble ash value	Water soluble ash value	Moisture content	pH value	
					1 %	10 %
Root	16.02	12.06	76.34	66.88	8.4 ± 0.2	6.8 ± 0.4
Stem	26.05	21.3	34.08	46.02	7.4 ± 0.3	5.7 ± 0.05
Leaves	18.01	21.62	23.94	75.62	7.5 ± 0.03	5.9 ± 0.01

Pharmacognostic (fluorescence) analysis

The powdered samples of *C. murale* showed some particular color differences, in case through using various chemical reagents and seeing them under visible light and UV light at short (254 nm) and long (366 nm) wavelengths. Such typical fluorescence interactions provide evidence of the existence of different phytochemical constituents which may be used as diagnostic parameters to authenticate and standardise the plant material (4). The color emission of the fluorescence of powdered roots, stems and leaves exposed to the various solvents, reagents and chemicals varied with the visible, low and high UV light. Table 3 shows the detailed observations.

Phytochemical analysis

Preliminary phytochemical screening revealed the presence of several bioactive constituents in different parts of *C. murale*. Among the tested solvents, the ethanolic extracts exhibited a comparatively higher abundance of phytoconstituents (Table 4) and were therefore selected for further investigations. Major secondary metabolites detected included alkaloids, flavonoids, phenolics, glycosides, tannins, carbohydrates, proteins, steroids and fixed oils in varying proportions across roots, stems and leaves. Leaf extracts showed a particularly rich profile of alkaloids, flavonoids and phenolic compounds, while roots also contained notable levels of flavonoids and glycosides. Stem extracts generally exhibited comparatively lower concentrations of several metabolites. The presence of phenolics and flavonoids is especially significant due to their well-documented antioxidant potential and role in neutralising free radicals, which may contribute to disease prevention and therapeutic effects (20–22).

Alkaloids, used in the pain relief, defense mechanisms and detoxification processes were discovered in different proportionalities in all parts. All the leaf extracts (except chloroform one) revealed a high alkaloid content and roots and stems showed traces only. Anthraquinones were present in all the leaf extracts with the exception of the chloroform extract and were found in lower levels in

Table 3. Fluorescence characteristics of powder of different parts (root, stem and leaves) of *Chenopodium murale*

Reagents used	Visible	Low UV (254 nm)	High UV (366 nm)
Root			
Original powder	Yellow	Light yellow	Yellow
Acetic acid	Slight yellow	Slight yellow	Pale yellow
Distilled water	Pale yellow	Yellow	Yellowish
1N HCL	Turbid white	White	White
1N H_2SO_4	Yellowish brown	Brown	Yellowish brown
1N $FeCl_3$	Light green	Pale green	Light green
Conc. HNO_3	Brown	Brown	Brownish
Iodine solution	Orange	Reddish	Reddish brown
Ammonia solution	Turbid yellow	Whitish yellow	Turbid yellow
1N NaOH	Light yellow	Pale yellow	Fluorescent yellow
Potassium dichromate solution	Saffron	Yellowish orange	Saffron
Methanol	Turbid white	Turquoise	Bluish white
Stem			
Original powder	Yellow	Bright Yellow	Yellow
Acetic acid	Pale white	Pale white	White
Distilled water	Pale yellow	Slight yellow	Slight yellow
1N HCL	Slight pale yellow	Slight pale white	Pale yellow
1N H_2SO_4	Brownish	Brownish black	Black- Brownish
1N $FeCl_3$	Green	Green	Dark Green
Conc. HNO_3	Light brown	Light brown	Dark brown
Iodine solution	Dark orange	Dark orange	Orange
Ammonia solution	Slight yellow	Slight yellow	Slight yellow
1N NaOH	Pale yellow	Pale yellow	Yellow
Potassium dichromate solution	Orangish	Orangish	Red- orangish
Methanol	Light yellow	Light yellow	Yellow
Leaves			
Original powder	Dark green	Dark green	Dark green
Acetic acid	Brown	Light brown	Brown
Distilled water	Pale green	Green	Fluorescent green
1N HCL	Slight black-brownish	Brownish	Brownish
1N H_2SO_4	Dark brown	Brown	Blackish
1N $FeCl_3$	Darkish green	Light green	Blackish green
Conc. HNO_3	Orange	Slight red	Fluorescent orange
Iodine solution	Brown	Brown	Slightly Brownish
Ammonia solution	Pale green	Mint green	Green

Table 4. Preliminary phytochemical screening of different parts (stems, roots and leaves) of *Chenopodium murale*

Plant Constituents	Test Performed	Stem						Roots						Leaves					
		PE	B	C	EA	E	AQ	PE	B	C	EA	E	AQ	PE	B	C	EA	E	AQ
Primary metabolites																			
Protein and amino acids	Biuret test	-	-	++	-	-	-	+	-	-	++	++	-	-	-	+	+	++	-
	Xanthoproteic test	++	+	+++	-	-	-	+	+	-	+	++	+	-	+	-	-	++	+
Carbohydrates	Molisch's test	-	+	-	-	-	-	-	-	+	-	-	+	+	-	-	+	+	++
	Fehling's test	-	++	-	-	+++	-	+	-	-	+	-	+	-	-	+	-	++	-
Fixed oils and fats	Saponification test	-	-	+++	-	-	-	-	-	-	+	-	-	-	-	-	+	-	+
Secondary metabolites																			
Alkaloids	Mayer's test	-	-	-	-	+	-	-	-	+	-	+	++	+	+	-	-	+	+
	Wagner's test	-	-	+	-	++	-	-	-	-	+	-	+	-	-	++	+	-	-
Anthraquinons	Hydroxy-anthraquinone test	-	-	-	-	++	-	-	-	-	-	-	-	+	+	-	+	+	+
Cardiac glycosides	Keller- killiani's test	-	+++	-	-	-	-	+	-	++	+	-	+	-	-	-	+	+	-
Flavonoids	Alkaline reagent test	+	-	+	-	-	+	+	+	++	-	+	++	+	-	+	+	++	-
Phenols	Potassium dichromate test	-	-	-	-	++	-	+	-	-	++	+	-	+	++	-	-	++	+
	Lead acetate test	+	-	-	-	+	-	-	++	+	-	-	+	-	-	-	+	+	++
Tannins	Ferric chloride test	+	-	-	+	++	+	+	-	-	++	+	-	+	+	+	-	-	+
	Vanillin HCL test	-	-	-	++	+	-	+	+	-	+	-	+	-	-	-	-	+	-
Phlobatanins	Folin-ciocalteau test	-	-	-	-	++	+	-	-	-	-	+	+	+	+	-	+	-	-
Polyphenols	Olive oil test	-	-	-	-	-	-	+	+	-	-	+	-	-	-	-	+	+	+
Steroids	Salkowski test	-	-	+	+++	-	-	+	+	++	-	-	+	+	-	+	++	+++	-

PE: petroleum ether; B: benzene; C: chloroform; EA: ethyl acetate; E: ethanol; AQ: aqueous extract of *Chenopodium murale*; (+) indicate the present while (-) indicates absent.

the roots and stems. Glycosides, which are common in the medicinal plants and have great therapeutic potential, were particularly represented in the petroleum ether, chloroform, ethyl acetate and aqueous root extracts with a low representation in the stem and leaves. Steroids and glycosides detected in the extracts further support the potential pharmacological relevance of the plant, including possible anti-inflammatory and immunomodulatory properties (23–25).

Overall, the higher concentration of phytochemicals observed in the ethanolic leaf extract suggests that this plant part may represent the most promising source of bioactive compounds, which is consistent with its subsequent antioxidant and antimicrobial performance observed in the study.

Characterisation of Zn-O-NPs and Fe-O-NPs

Visual observation

The outstanding optical properties of nanoparticles result in their significant appeal in scientific attention. The change in colour during the formation of nanoparticles is one of the major signatures of nanoparticle synthesis. Zn-O-NPs and Fe-O-NPs synthesis in freshly prepared extracts of *C. murale* was also established by a perceptible color change i.e., green to yellow in case of Zn-O-NPs and green to brown in case of Fe-O-NPs. The observed visual transformation indicates the purification of the metal ions into nanoparticles and their further aggregation into colloidal systems due to the reducing effect of the phytochemicals phenolics and terpenoids in the plant extract. The surface plasmon resonance (SPR) is the reason behind the brown coloration of Fe-O-NPs (26). Likewise, Zn-O-NPs have been prepared by the use of the extract of aerial parts of *Deverra tortuosa* which is a natural extract that is eco-friendly and serves as a reducing and stabilising force. During it, the change of the color of the solution and the appearance of the yellowish-white precipitate proved the decrease of zinc nitrate to Zn -O-NPs (27).

UV-visible analysis

One of the most relevant methods of analysing the optical properties of nanoparticles is UV-visible analysis. The absorption peaks of Zn-O-NPs and Fe-O-NPs were observed in the wavelength of 250–400 nm in the present work. The peaks of 353 nm in the case of Zn-O-NPs and 311 nm in the case of Fe-O-NPs (Fig. 3) are ascribed to the SPR effect, which proves the successful production of the nanoparticles. Likewise, the Zn-O-NPs prepared using *Scutellaria baicalensis* root extract was found to have the highest absorbance at a wavelength of 316 nm, which indicates the formation of nanoparticles (28). Balogun et al. (29) explain that Zn-O-NPs made using *Mimosa pudica* leaf extract had several peaks at 235, 250, 270 and 300 nm which were relatively lower than the bulk Zn-O-NPs which are generally observed at 350 nm within the visible light region.

In the case of Fe-O-NPs, the UV spectrum of the 01 : 01 concentration showed a distinct absorption at 380 nm, which indicates that there was Fe-O-NPs. As documented, Fe-O-NPs exhibit intense absorption at wavelengths between 320 and 420 nm, which is associated with a band gap at about 2.1 eV. The observed 380 nm peak corresponds well with the reported literature on Fe-O-NPs (30) and the results of SPR vibrations depending on the size, shape and surface modification of nanoparticles (31). Such SPR peaks are a key parameter to explain the physicochemical properties and possible uses of Fe-O-NPs in various fields including catalysis and biomedical research (32).

X-ray diffraction analysis

X-ray diffraction is a powerful and the most used analytical tool in studying structural aspects of different materials including magnetic nanoparticles (33). The XRD analysis was conducted in the given study to identify the structural character of the

nanoparticles that were synthesised. The achieved diffraction patterns are shown in Fig. 3 a and b. The diffraction pattern shows that there are a number of sharp and sharp peaks at certain 2θ values (2θ = 25°, 28°, 31°, 34°, 36°, 40°, 47°, 56° and 62°) which were indexed to the corresponding crystal planes (100), (002), (101), (102), (110), (103), (112), (200) and (201), confirming the crystalline structure (Fig. 3a) and yielding an average crystallite size of Zn-O-NPs in the range of ~20–35 nm. The observed peaks are consistent with standard JCPDS reference patterns, indicating phase purity without detectable secondary phases. On the other hand has a broad hump and not sharp peaks similar to a typical amorphous crystalline substance (Fe-O-NPs) (Fig. 3b). The broad halo that is identified in the region between 2θ = 20°-30° indicates the absence of long-range structural order thus validating the amorphous character of the material. It is possible to observe these contrasting diffraction patterns that reveal very clearly the structural differences between crystalline nanoparticles (Fig. 3a) and amorphous materials (Fig. 3b). Crystallinity is a critical parameter because it has an effect on various physicochemical and biological properties of nanomaterials. Crystalline Zn-O-NPs and Fe-O-NPs are expected to be more stable, show higher catalytic potential and antimicrobial effect due to their ordered structure in comparison to their amorphous counterparts.

The XRD peaks of the Zn-O-NPs synthesized with the help of *Peganum harmala* seed extract were identified at different 2 the values as 32.22 (100) owing to 100, 35.01 (002) owing to 002, 36.80 (101) owing to 101, 48.31 (102) owing to 102, 57.46 (110) owing to 11 Debye-Scherrer equation was used to compute the mean particle size of biosynthesized Zn-O-NPs by *Fussarium officinalis* and *P. harmala* extracts (29).

Likewise, the crystallite size of Fe-O-NPs calculated through the Debye-Scherrer equation was estimated to be about 16 and 12 nm in the 01:01 ratio and 01:04 ratio respectively (34, 35). The sizes of the particles were dependent on the concentration, but the crystalline characteristics were similar in all samples. The crystalline structure of Fe-O-NPs is an important factor in determining their magnetic, structural and size-dependent properties. Various crystal structures of FeO, including magnetite (Fe_3O_4), maghemite (g-Fe_2O_3) and hematite (g-Fe_2O_3) have diverse magnetic properties because of differences in their crystal structure, which directly influence many of their magnetic properties including magnetization, super-paramagnetism and interparticle magnetic interactions (36).

Fourier transform infrared analysis

Fourier transform infrared is an important form of analysis to recognise characteristic peaks and functional groups of bioactive compounds through the analysis of their absorption in the infrared region. The FT-IR analysis in this research determined that different phytochemical constituents naturally occur in the metabolism of plants. These biomolecules are reducing and stabilising factors in the biosynthesis of Zn-O-NPs and Fe-O-NPs as revealed by their unique spectral characteristics. The identified peaks are due to the vibrational movements of the molecular bonds, which proves the formation of various functional groups during the formation of nanoparticles.

The recorded FT-IR spectra showed absorption bands ranging between 500–4000 cm^{-1}. A broad peak observed at 3278.74 and 2356.14 cm^{-1} corresponds to O–H stretching vibrations of carboxylic acids. Additional peaks detected at 1015.28–1030.73, 1278.50, 1355.77–1435.67 and 1629.88–1652.83 cm^{-1} represent C–H bending, C–N stretching, C–O stretching, CH_2 bending and C=C stretching vibrations, respectively, the latter indicating aromatic ring structures. A weaker signal around 799.39–807.79 cm^{-1} was assigned to C-Cl stretching (Fig. 3).

The characteristic peaks related to amides, amines and aromatic amines all changed to 1602, 997 and 1247 cm^{-1} in the FT-IR spectrum of the *S. baicalensis* root extract after the synthesis of Zn-O-NPs. The changes indicate that the interactions of these functional groups with the Zn-O-NPs are likely to occur and hence, they are involved in reducing zinc nitrate to Zn-O-NPs (28).

Similar FT-IR findings were also related to the synthesis of Fe-O-NPs in the presence of *Ficus carica* L. fruit extract, which proved the possibility of using plant-derived compounds in the environmentally friendly synthesis of Fe-O-NPs (37). The FT-IR is therefore an important method of establishing the functional groups that are on the surface of nanoparticles that is a very useful information concerning their surface chemistry and potential use (32). The functional groups found in this study will be thought to provide stabilisation of the nanoparticles by steric, electrostatic forces and by a specific chemical bond to the nanoparticle surface. All these processes contribute to the regulated production of Fe-O-NPs and an increase in their stability in the biosynthetic process (33).

Particle size

The particle size is an important factor that affects the adhesion of nanoparticles to fibrous fibres like cotton and wool. Smaller NPs have increased interaction with microbial cells. The size confirmation was initially done by performing the zeta size analysis that indicated that the Zn-O-NPs had an average size of 190 nm, whereas the Fe-O-NPs had a size of approximately 189 nm with good quality reports. The polydispersity index (PDI), which is used to determine homogeneity and stability of nanoparticles, is very fundamental in the evaluation of nanoformulations. A value of PDI below 0.7 indicates high colloidal system stability or nano-delivery formulation. Nanoparticles once synthesised tend to have differences in size and surface chemistry hence it is difficult to have homogeneity. The particle size distribution histogram showed that the biosynthesised Fe-O-NPs was found to have a diameter of between 10 and 80 nm with the average diameter being 42.327 nm (38). The values of PDI of Zn-O-NPs and Fe-O-NPs in the current study were found to be 0.238 and 0.423, respectively that indicate acceptable colloidal stability and moderate size distribution of the biosynthesised nanoparticles. However, the chain-like aggregation observed in TEM images may be attributed to interparticle interactions and magnetic or surface forces during drying, which can promote partial clustering despite the overall stable dispersion. Such aggregation is commonly reported in biosynthesised metal oxide nanoparticles and does not significantly compromise their nanoscale characteristics (38) (Fig. 4).

Field emission scanning electron microscopy, energy-dispersive X-ray analysis and transmission electron microscopy analyses

The FE-SEM is a vital characterisation methods that are highly applied in the field of materials science and nanotechnology. The FE-SEM is based on the principle of irradiation of the specimen by a concentrated electron beam on the surface that creates high-resolution images, which makes it possible to analyse the surface structure, texture and morphology of the specimen in detail. Conversely, EDX supplements this by determining and measuring

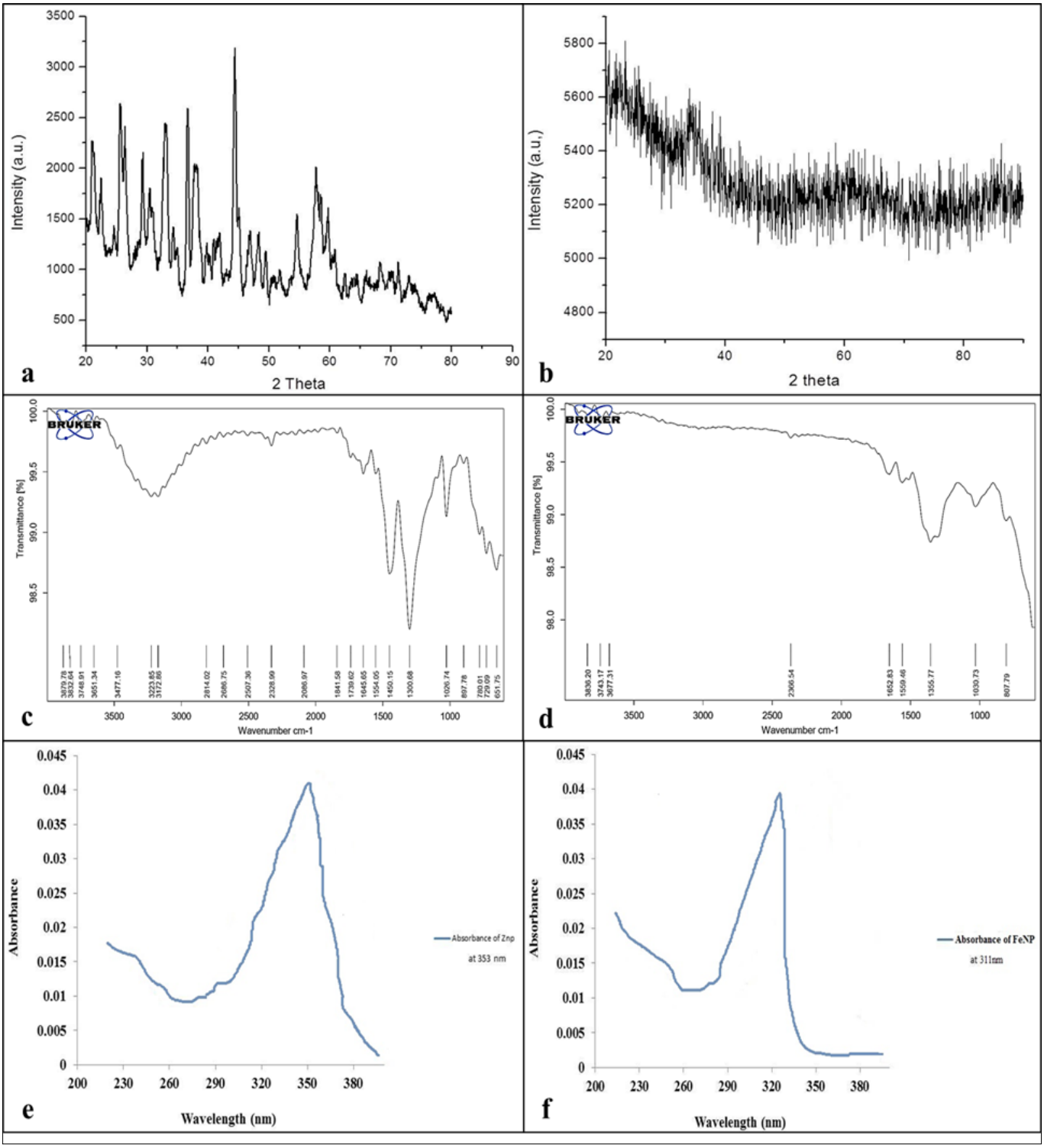


Fig. 3. Characterisation of biosynthesised nanoparticles from *Chenopodium murale*. X-ray diffraction (XRD) spectra: (a) Zn-O-NPs; (b) Fe-O-NPs. Fourier transform infrared (FT-IR) spectra: (c) Zn-O-NPs; (d) Fe-O-NPs. UV-visible graph (e) Zn-O-NPs at 353 nm; (f) Fe-O-NPs at 311 nm.

the composition of the sample in terms of elements, on the basis of the distinctive X-rays produced when the material is subject to the electron beam. FE-SEM along with EDX provide detailed data on the physical and chemical characteristics of nanomaterials and, therefore, these two methods are irreplaceable in the process of characterising and analysing materials (33).

The images of FE-SEM indicated that the images of the synthesised Zn-O-NPs and Fe-O-NPs had an approximate diameter of between 50 and 80 nm with slight differences. According to the observations made at magnifications ranging from 1 µm to500 nm, mostly the morphologies were spherical and in some cases the morphologies were hexagonal (Fig. 4). The presence of both shapes can be explained by the fact that organic compounds as capping or stabilising agents are performing their role in the synthesis process. Elemental composition - EDX spectra confirmed the existence of other elements other than zinc, which implied other elements in the plant extract had been absorbed into the nanoparticles.

The formation of these metal oxide nanoparticles was confirmed by the EDX analysis of both the synthesised Zn-O-NPs and Fe-O-NPs as they did contain their constituent elements i.e., zinc and oxygen in the case of Zn-O and iron and oxygen in the case of Fe-O-NPs. Other elements also formed minor peaks, which can have been formed by plant-derived biomolecules or other impurities, so the nanoparticles were not in their pure form. In another similar study, EDX spectra of Fe-O-NPs had strong absorption peaks to indicate the presence of iron at 0.7, 6.4 and 7

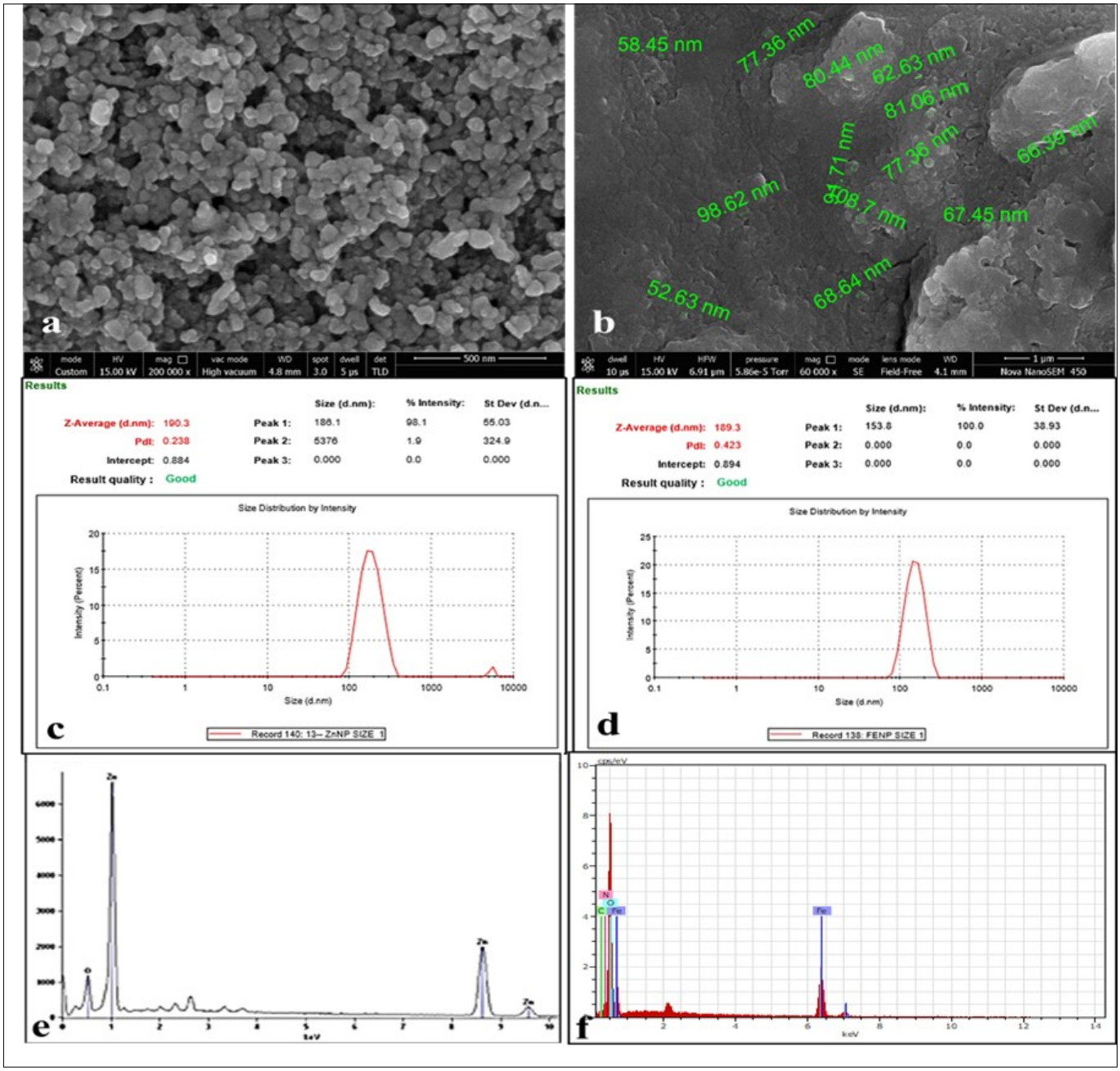


Fig. 4. Field emission scanning electron microscopy (FE-SEM) analysis, particle size distribution and energy-dispersive X-ray (EDX) spectra of biosynthesised nanoparticles from *Chenopodium murale*. FE-SEM images: (a) Zn-O; (b) Fe-O-NPs. Particle size distribution graph: (c) Zn-O; (d) Fe-O-NPs. EDX spectra: (e) Zn-O; (f) Fe-O-NPs.

keV (89.5 % of total sample composition) whereas oxygen and sodium were found to have 0.5 and 1 keV, respectively (33).

The TEM gave further nanoscale information; it was visualised to see the internal structure, size and morphology of the synthesised nanoparticles by passing an electron beam through ultra thin samples. The TEM analysis was used to determine the size of the Fe-O-NPs and the size was in the nanometric range of between 7 and 37 nm with an average diameter of 24.32 ± 5.03 nm. The size distribution histogram indicated that the distribution of the most common particles was between 25 and 27 nm and it consisted of approximately 18.64 % of the sample (33). Images of TEM further confirmed that Zn-O-NPs and Fe-O-NPs, which were synthesised by bioreduction with the help of plants, had diameters of core about 50 nm and 20 nm, respectively and were of nearly spherical morphologies (Fig. 5). Aglomeration effects to some extent were witnessed, in the form of chain like structures of nanoparticles. The variation in particle size observed between zeta size, TEM and FE-SEM analyses may be attributed to differences in measurement principles. Zeta size measures the hydrodynamic diameter of nanoparticles in suspension, which includes the solvation layer and possible agglomeration, resulting in larger apparent sizes, whereas TEM and FE-SEM provide the actual physical core size of dried nanoparticles. Therefore, the comparatively smaller sizes observed in TEM and FE-SEM are consistent with the nanoscale morphology of the synthesised particles.

The Zn-O-NPs typically existed in the form of aggregated, cotton-like formations, which was in accord with the previous report on Zn-O-NPs synthesis in plants. Likewise, FE-SEM and TEM of Zn-O-NPs synthesised using the root extract of *S. baicalensis* revealed that the morphologies of the material were mainly spherical and irregular. TEM especially gave the accurate dimensions of the particles meaning that the particles of Zn-O-NPs were between 33.14 and 99.03 nm in size (28).

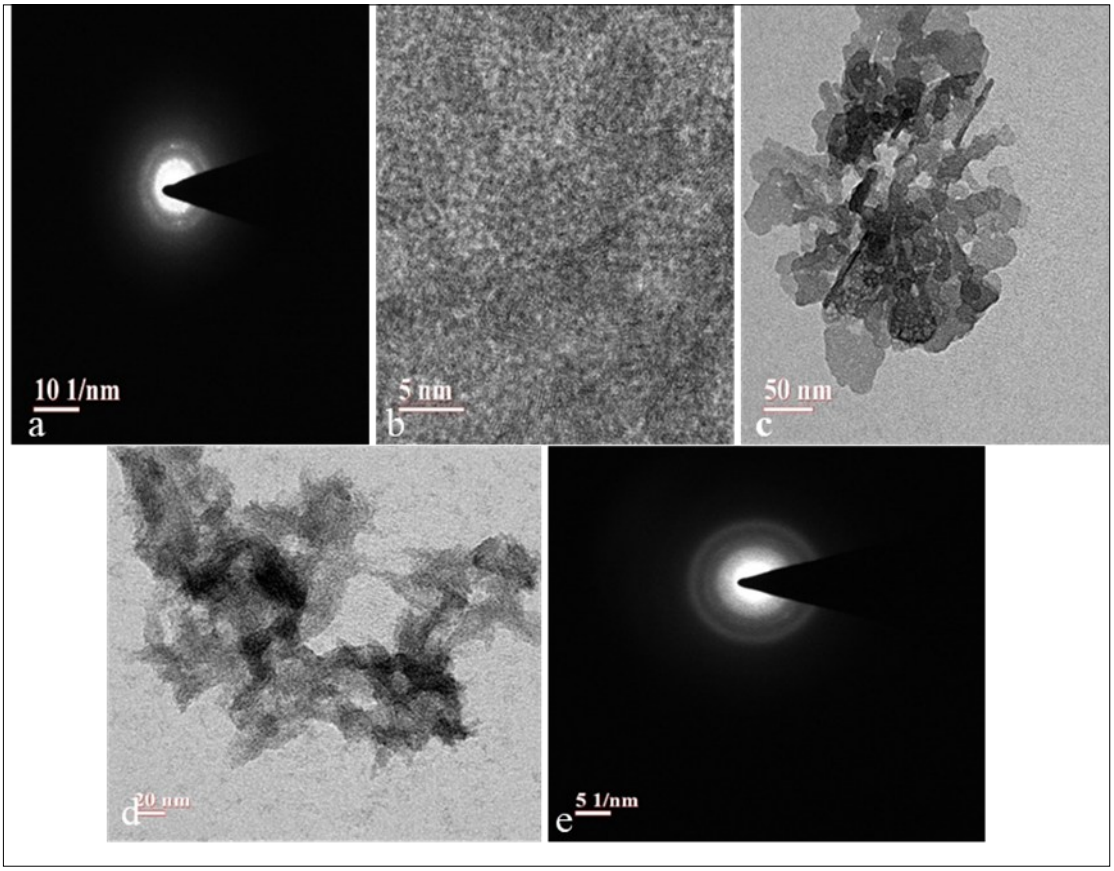


Fig. 5. Pictorial representation of transmission electron microscopy (TEM) analysis of biosynthesised nanoparticles from *Chenopodium murale*. (a, b, c) Zn-O-NPs; (d, e) Fe-O-NPs.

Determination of antioxidant activity

The consistent production of free radicals and the so-called reactive oxygen species (ROS) can cause massive damage to cells in the biological system and eventually, it may result in the development of many diseases (39). The current study evaluated the antioxidant (free radical scavenging) and biochemical constituents of *C. murale*. Free radicals are considered to play a central role in the development of diseases such as cancer, neurodegenerative disorders and acquired immunodeficiency syndrome (AIDS); therefore, antioxidants that neutralise these reactive molecules are believed to be beneficial in the prevention and management of such diseases.

2,2-Diphenyl-1-picrylhydrazyl activity of crude ethanolic extract

The DPPH free radical assay is a very sensitive technique that determines the antioxidant potential of the plant extracts. It is the method used to determine the capacity of a sample to donate the hydrogen atoms to the DPPH radical which in turn causes a change in colour of the solution to change the deep violet solution to a light yellow. Antioxidant efficiency is a percentage of the inhibition which is proportional to the concentration of the sample. An increase in the degree of inhibition is an indication of an increase in the free radical scavenging activity. In the current research study, both AA and the ethanolic leaf extract gave a 50 % scavenging activity when tested at a concentration of 0.4 mg/mL, although the standard had slightly higher values than the test extract. These results validate that the plant leaves have some significant antioxidant activities. In addition to that, the DPPH scavenging activities were compared and the test extract showed approximately 30 times lower than the standard, at 1.0 mg/mL, which means that it has moderate, though effective, free radical neutralising activities.

2,2-Diphenyl-1-picrylhydrazyl activity of biosynthesised nanoparticles

The capacity of a sample to give the hydrogen atom to DPPH radical causes the decolorisation of the DPPH solution of deep violet into light yellow. The percentage of inhibition, in which the antioxidant efficiency was put across, was found to be dose-dependent indicating increasing levels of scavenging activities with increase in concentration. The sample that contained the most percentage of inhibition implied better radical scavenging potential. Of all the samples tested, Zn-O-NPs resulted in 50 % scavenging activity with a 0.4 mg/mL concentration and Fe-O-NPs had the same activity at 0.6 mg/mL. The Soxhlet extract of ethyl acetate leaf extract was found to have a 50 % activity at 0.8 mg/mL and the ethanol extract was found to have the same activity at 0.4 mg/mL. A general trend in relation to the antioxidant potential was in the order Zn-O-NPs (76.28 %) > Fe-O-NPs (73.84 %) > ethanolic leaf extract (67.08 %) (Fig. 6a), emphasising the possible role of surface reactivity, higher ROS generation and enhanced interaction of Zn-O-NPs with phytochemical capping agents that may contribute to improved radical scavenging efficiency.The DPPH scavenging ability was proportionate to the concentration of the plant extract and also the Zn-O-NPs of *Salix tetrasperma* Roxb. (willow plant). The scavenging efficiency of the plant extract and Zn-O-NPs was 93.0 and 93.6, respectively, at 1000 µg/mL. The existence of phenolic compounds and flavonoids that have been reported in *S. tetrasperma* might explain the antioxidant activity of the plant extract (40).

Moreover, Fe-O-NPs with antioxidant properties can be highly promising to be applied in the biomedical field of drug delivery, targeted therapy, cancer therapy, as well as antioxidant stress defense. Their robust antioxidative property increases their application in specific delivery systems, which further provides

novel opportunities in the management of oxidative stress when it occurs in the *in vivo* environment (41). The recent trends in research are about the establishment of environmentally-friendly nanoparticles possessing enhanced antioxidant activities.

Ferric reducing antioxidant power assay of crude ethanolic extract

The antioxidant capacity of a sample is determined by its capacity to reduce ferric ions (Fe^{3+}) to ferrous ions (Fe^{2+}). In the process of reduction, the FRAP reagent turns to deep violet, which is an indication that 2,4,6-tripyridyl-s-triazine (TPTZ) has been reduced. The FRAP assay has a concentration based relationship in which the antioxidants activity increases with the sample concentration. It is this reducing ability that is credited to the presence of reductones which are compounds that are known to be antioxidants by being known to contribute hydrogen atoms thus disrupting the chain reaction of free radicals (42).

The peroxide precursors also react with redalkene resulting in the inhibition of the peroxide formation. The reducing power is studied in the sample extract and its contribution to the antioxidant activity is demonstrated. The maximum reducing power of ferric ions by the ethanol leaf extract was 5.80, which is higher than that of the standard, might be attributed to the presence of polyphenols and flavonoids with strong reducing capacity. As in the case of the antioxidant trend, the reducing ability of the ethanolic extract was observed to rise steadily as the sample concentrations rose (Fig. 6b).

Metal chelation activity of crude ethanolic extract

The existence of other metal-binding agents may break the formation of the ferrozine-Fe^{2+} complex. The reaction of ferrozine with ferrous ions yields a red colour of this reaction, but this colour disappears in the presence of a chelating agent, hence, showing that it is capable of binding iron. The extent of colour decrease is an indication of how well the sample chelates (43). This assay showed that both the plant extract and the standard compound could inhibit the development of the ferrous-ferrozine complex and this proves that the two have metal-chelating potential because they manage to trap the Fe^{2+} ions before complexation. The concentration of the samples was proportional to the percentage of chelating activity. EDTA was used as the reference standard. The reduction in the color intensity of ferrozine complex in the presence of an antioxidant compound indicated the chelating capacity of the sample, which is also an indicator of the antioxidant strength as well. The crude ethanolic extract appeared to have a highest reducing capacity of complex of 4.55 as compared to EDTA (Fig. 6b). The antioxidant effect observed is probably correlated to an iron-binding activity of the extract.

Antimicrobial activity

The antimicrobial susceptibility can be defined as the power of nanoparticles to inhibit or oppose the development of micro-organisms like bacteria and fungi. The bacteria species may be either Gram-positive with a thick peptidoglycan cell wall that is relatively difficult to break or Gram-negative with the thinner layer of the peptidoglycan that can easily be penetrated. Evaluation of antimicrobial activity is also done on nanoparticles against different strains of fungi.

Antibacterial assay

It was found that both Zn-O-NPs and Fe-O-NPs had a significant antibacterial effect on different bacterial strains at different concentrations. Maximum inhibition levels (comprising of 0.2 mg/mL, 0.8 mg/mL and 1 mg/mL) were 34 mm, 28 mm and 20.66 mm against *E. coli* (Gram negative), *B. subtilis* (Gram positive) and *P. aeruginosa* respectively. The smallest inhibition zones were used to measure 0.2 mg/mL and the largest ones were 1.0 mg/mL (Fig. 7a–i).

The Zn-O-NPs have been observed to have a strong potential of antibacterial activity to both Gram-positive and Gram-negative bacteria. This is mainly due to the production of antimicrobial effects through the creation of the so-called ROS that result in oxidative stress and subsequent bacterial cell death (44). Zn-O-NPs synthesised biologically have shown increased antimicrobial responses and are of interest to be incorporated on the future antimicrobial preparations. Previous researchers also found that Zn-O-NPs made with the willow plant (*S. tetrasperma*) had a significant antibacterial activity with an inhibition zone of 28.10 mm, 23.83 mm, 28.33 mm, 23.83 mm, 28.33 mm and 33.83

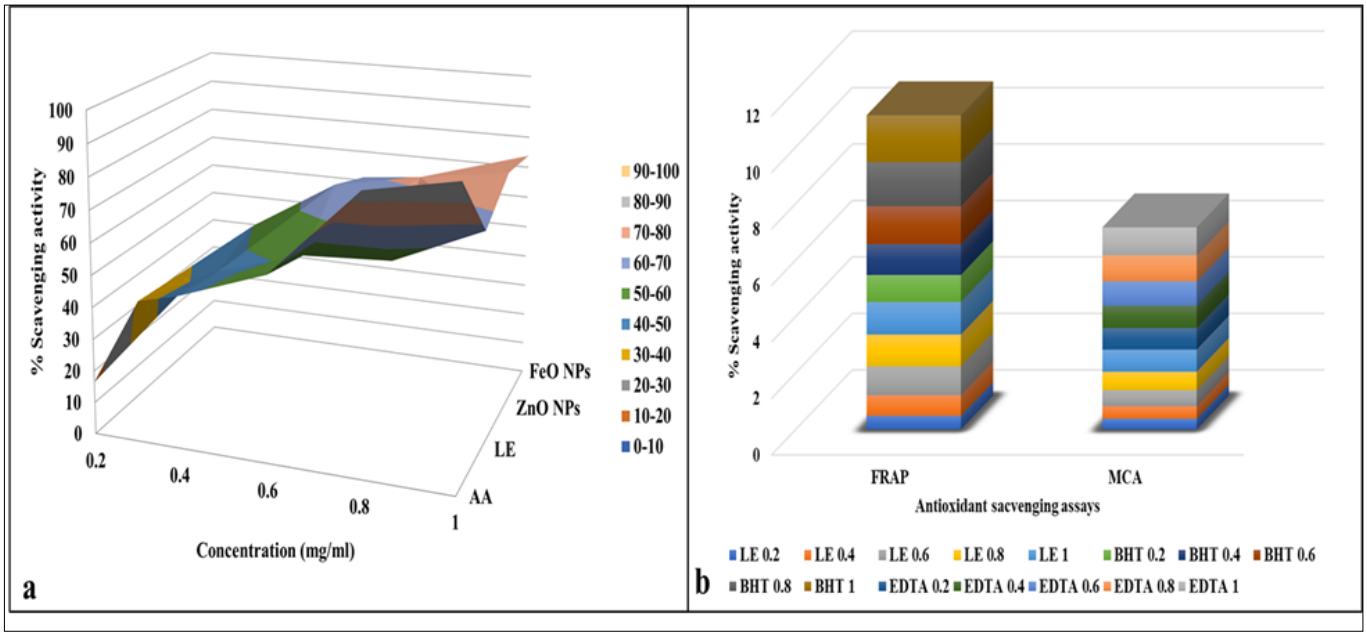


Fig. 6. Antioxidant activities of leaf ethanolic extract (LE) and biosynthesised nanoparticles (Zn-O-NPs and Fe-O-NPs) from *Chenopodium murale* at different concentrations. (a) DPPH free radical scavenging assay; (b) ferric reducing antioxidant power (FRAP) and metal chelating activity (MCA) activity.

mm against *B. subtilis* (45). Likewise, synthesised Fe-O-NPs with *Pseudomonas fluorescens* were tested on their antimicrobial activity against *Salmonella enterica*, *E. coli* and *S. aureus*, which are pathogens of significant disease burden during medical and food-borne diseases (46, 47). The Fe-O-NPs were identified to interfere with bacterial membrane, induce oxidative stress and damage membrane integrity by oxidation, surface pit formation and permeability change. They had different poisonous effects on various species of microbes. The antibacterial process has various pathways, namely, membrane damage, ribosome breakdown, enzyme blockage, protein denaturation and electron transport chain interference. The dissimilarity between the inhibition zone dimensions is probably the result of the disparities in cell wall structure and thickness of the bacterial species. Generally, the produced Fe-O-NPs showed robust effectiveness against the multidrug-resistant pathogens and their use is justified by the favourable physicochemical properties and multi-modal action mechanism (33).

Antifungal assay

Both, Zn-O-NPs and Fe-O-NPs showed great antifungal properties against *A. niger* and *P. chrysogenum*. The synthesised nanoparticles had better inhibitory effects compared to those of the ethanol leaf extract of *C. murale*. These were the most obvious and clear areas of inhibition of Zn-O-NPs at the concentrations of 0.2, 0.8 and 1.0 mg/mL, which were found to be more efficient compared to the rest of the concentrations. With Fe-O-NPs, the 0.4, 0.8 and 1.0 mg/mL concentrations had greater antifungal activity when compared to *P. chrysogenum*. In the case of *A. niger*, Zn-O-NPs exhibited the most powerful inhibitory effect in an equivalent level of concentration and Fe-O-NPs had the comparatively low antifungal capacity. The

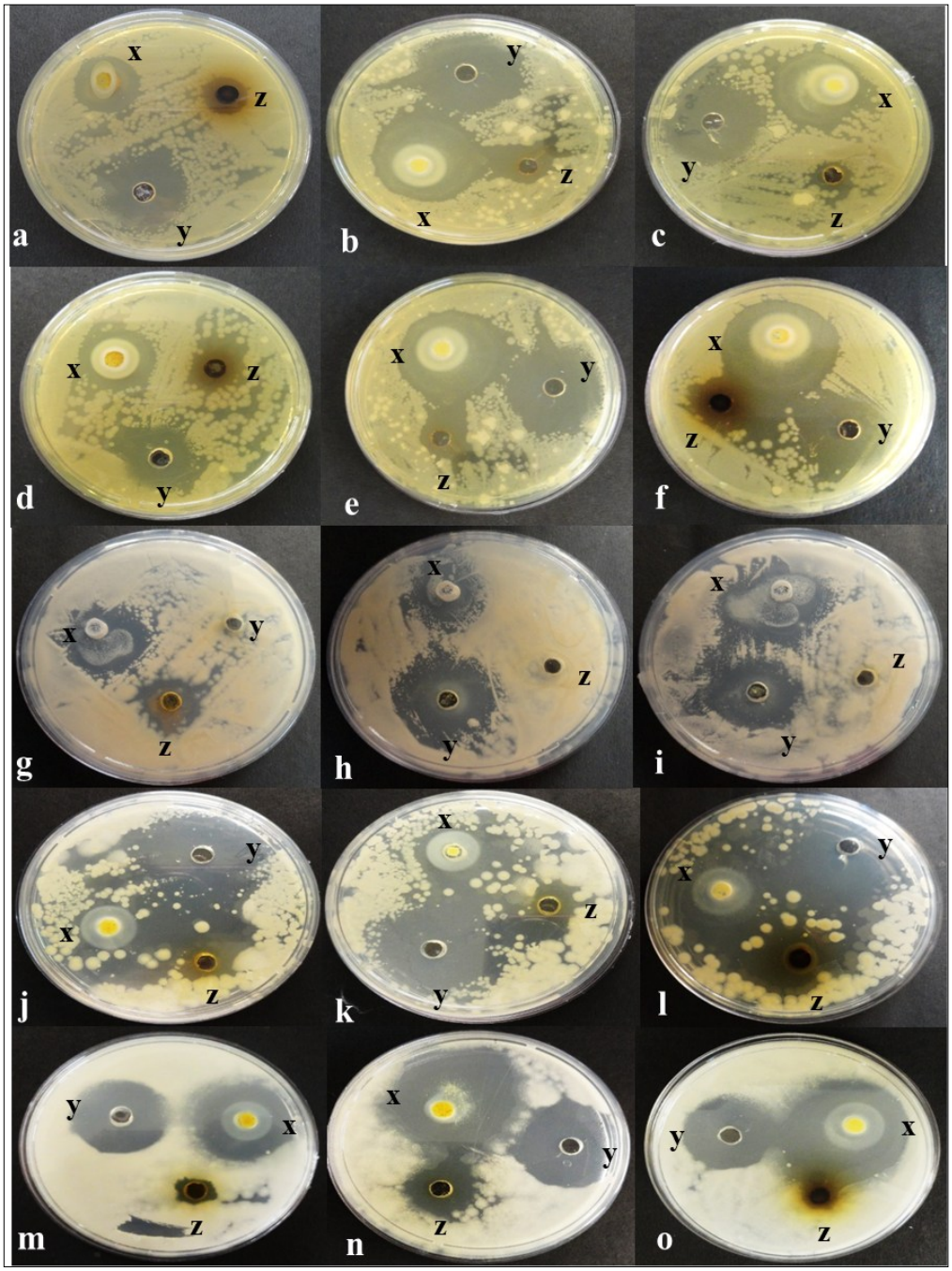


Fig. 7. Disc diffusion-based antimicrobial activity of biosynthesised nanoparticles from *Chenopodium murale* against Gram-positive, Gram-negative bacterial and fungal strains at concentrations of 0.6, 0.8 and 1.0 mg/mL, respectively. Antibacterial activity against: (a–c) Gram-positive *Bacillus subtilis*; (d–f) Gram-negative *Escherichia coli*; and (g–i) Gram-negative *Pseudomonas aeruginosa*. Antifungal activity against: (j–l) *Aspergillus niger* and (m–o) *Penicillium chrysogenum*. Microplate identifiers: x (Zn-O-NPs), y (Fe-O-NPs) and z (ethanolic leaf extract).

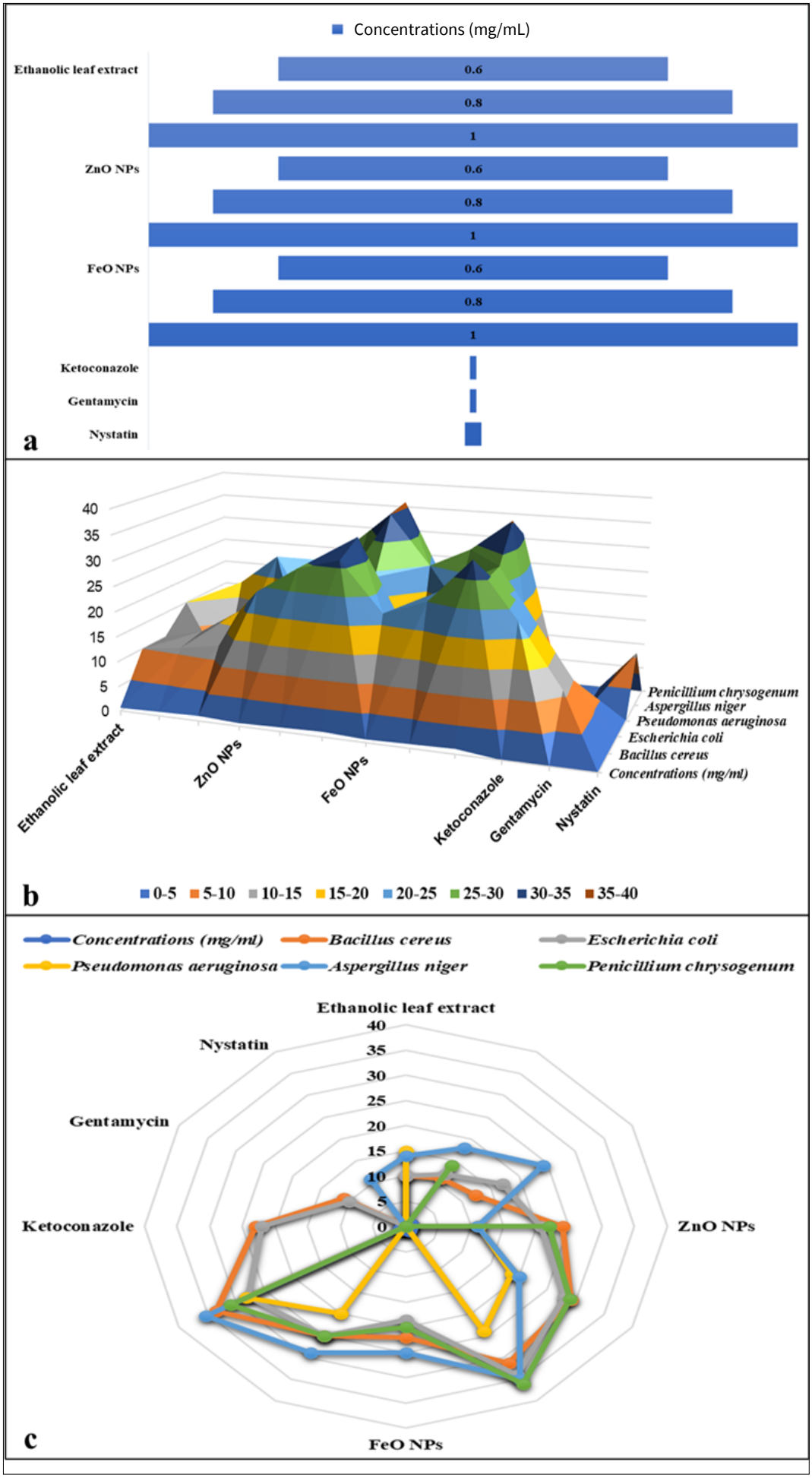


Fig. 8. Graphs showing the inhibition zone diameter of ethanolic leaf extract and biosynthesised nanoparticles (Zn-O-Nps and Fe-O-NPs) from *Chenopodium murale* against bacterial and fungal strains. (a) Funnel map; (b) surface plot; (c) radar map.

largest range of inhibition of Fe-O-NPs against *A. niger* was observed at 0.8 and 1.0 mg/mL (Fig. 7 j–o). Fig. 8 shows the graphs for the inhibition zone diameter of ethanolic leaf extract and biosynthesised nanoparticles (Zn-O-NPs and Fe-O-NPs) from *C. murale* against bacterial and fungal strains.

The research has proposed that, Fe-O-NPs may damage fungal cell membrane by direct contact or electrostatic interaction with the fungal cell surface, by internalisation into the fungi cells and by producing so-called ROS including hydrogen peroxide generated by metal oxides. The Fe-O-NPs exhibit high surface-to-volume ratio hence stick firmly onto the fungal cell walls and may penetrate directly, resulting in structural disintegration. Their antifungal effect is mainly through interference with the membrane permeability as well as causing oxidative stress, which prevents cell proliferation and eventually resulting to cell death. The mechanisms involved in fungal cell damage are the ROS generation which results in lipid peroxidation and physical embedding and adsorption that result in rupture of the cell wall and cell membrane, the development of pores, release of DNA and intracellular contents, release of ion, binding and condensation of DNA, altered gene regulation and dysfunction of the mitochondrion by releasing cytochrome-C leading to apoptosis. Also, Fe-O-NPs disrupt the structure of ribosomes and bind to extracellular polymeric materials, thereby inhibiting biofilm formation (48).

Broth-dilution method (Minimum inhibitory concentration determination)

The lowest concentration at which a substance can be used to inhibit growth of microorganisms is known as minimum inhibitory concentration (MIC). The inhibitory thresholds of Zn-O-NPs and Fe-O-NPs were obtained in mg/mL concentrations in this study. In the case of *P. aeruginosa*, both nanoparticles had low inhibitory concentrations of 0.2 mg/mL and high with 1.0 mg/mL. In the same way, the Fe-O-NPs were least effective against the *E. coli* at 0.2 mg/mL and the maximum inhibition of the *E. coli* was at 1.0 mg/mL. In general, Zn-O-NPs showed the highest antimicrobial potential with respect to *E. coli*, whereas Fe-O-NPs had a lower antimicrobial potential against the same strain (Fig. 9).

Similarly, the MIC value of Fe-O-NPs obtained against *Klebsiella pneumoniae* was described as 3.12 mg/mL and sub-MIC levels of inhibited biofilm formation effectively as the highest rate of inhibition was found to be 66.86 % at 1/2 MIC (49). In the case of Zn-O-NPs, MIC and minimum bactericidal concentration were found to be 31.25 ug/mL and 62.5 ug/mL, respectively (50).

Conclusion

The present investigation established pharmacognostic and physicochemical standards for the proper identification and quality evaluation of *Chenopodium murale*. Phytochemical screening indicated the presence of diverse secondary metabolites, particularly in the ethanolic leaf extract, which may contribute to the observed antioxidant activity. These bioactive compounds are known to contribute to free radical scavenging and may play an important role in mitigating oxidative stress. The study demonstrated the integrated pharmacognostic characterisation of *C. murale* with its application in plant-based synthesis of zinc oxide nanoparicles (Zn-O-NPs) and iron oxide nanoparticles (Fe-O-NPs) and evaluation of their bioactivities. The biosynthesised nanoparticles exhibited characteristic absorption peaks, spherical morphology and notable antimicrobial and antifungal activities, showing greater efficacy than crude plant extracts. These findings suggest that plant-mediated synthesis offers a sustainable and environmentally friendly approach for nanoparticle production with potential biomedical applications. Overall, the results highlight *C. murale* as a promising bioresource for phytochemical exploration and eco-friendly nanoparticle synthesis. Further investigations involving advanced structural characterisation, standardisation of synthesis protocols, *in vitro* and *in vivo* studies and biocompatibility assessments are necessary to better understand the mechanisms of action and to validate their therapeutic potential for pharmaceutical and biomedical applications. Therefore, detailed biocompatibility studies are recommended as an important direction for future research.

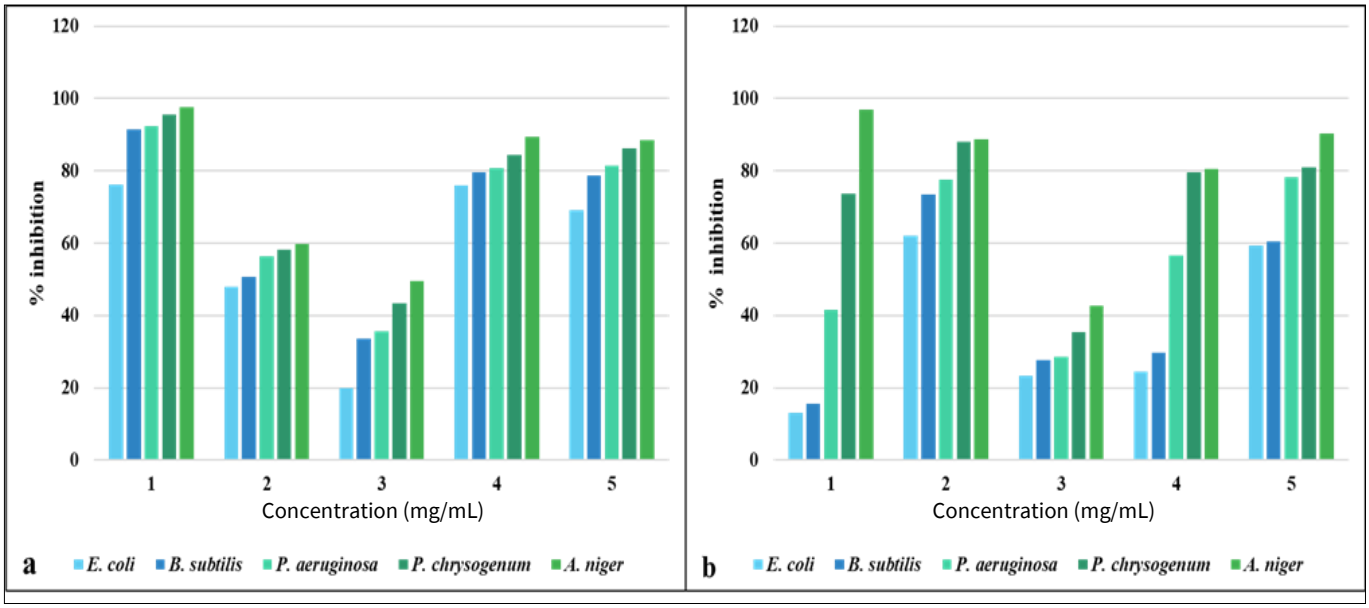


Fig. 9. MIC values of biosynthesised nanoparticles from *Chenopodium murale* against Gram-positive (*Bacillus subtilis*), Gram-negative (*Escherichia coli* and *Pseudomonas aeruginosa*) bacterial and fungal (*Aspergillus niger* and *Penicillium chrysogenum*) strains at concentrations of 0.2, 0.4, 0.6, 0.8 and 1.0 mg/mL: (a) Zn-O-NPs; (b) Fe-O-NPs.

Acknowledgements

The authors would like to warmly thank Vice-Chancellor of Banasthali Vidyapith, Rajasthan for providing excellent research facilities. They also acknowledge the Bioinformatics Center, Banasthali Vidyapith supported by DBT and DST for providing computation and networking support through the FIST and CURIE programs at the Department of Bioscience and Biotechnology, Banasthali Vidyapith, Rajasthan.

Authors' contributions

DK carried out the methodology and investigation, managed the resources, collected the data and drafted the original manuscript. MS, PC and PS contributed to the conceptualisation, provided resources and assisted with editing and data curation. AP participated in the revision, editing and visualisation of the manuscript. PJ contributed to the review, editing, investigation, visualisation, conceptualisation and supervision of the study. All authors have read and approved the final manuscript.

Compliance with ethical standards

Conflict of interest: Authors do not have any conflict of interests to declare.

Ethical issues: None

References

1. Jain D, Uniyal N, Mitra D, Janmeda P. Traditional resources and use of aromatic and ethno-medicinal plants in Uttarakhand: compliment of nature. Int J Herb Med. 2020;8(5):88–95.
2. Rehman T, Rao H. *Chenopodium murale* L.: A weed of medicinal importance-A brief review. Tradit Integr Med. 2023;8(4):397–407. https://doi.org/10.18502/tim.v8i4.14488
3. Kumari D, Janmeda P. Nanoparticles and phytoconstituents from marine mangrove plant. In: Shaju SS, Vipin PM, Visakh PM, editors. Marine Biotechnology. 2025. https://doi.org/10.1002/9781394301324.ch6
4. Janmeda P, Kumari D, Meena M, Prakash A. Comparative pharmacognostical evaluation, drug standardization and quality assurance from different parts of *Tribulus terrestris* L. Rev Food Agric. 2025;6(1):1–16. https://doi.org/10.26480/rfna.01.2025.01.16
5. Prakash A, Jain D, Tripathi R, Janmeda P. Pharmacognostical analysis of different parts of *Cyperus rotundus* L. Plant Sci Today. 2019;6:607–12. https://doi.org/10.14719/pst.2019.6.sp1.679
6. Kulkarni DS. Investigation of physicochemical composition of *Sceliphron caementarium* (black and yellow mud dauber) nest. Environ Conserv J. 2020;21(1-2):137–40. https://doi.org/10.36953/ECJ.2020.211216
7. Chaudhary P, Meena M, Janmeda P. Microscopic characterization, TLC fingerprinting and optimization of total lipid content from *Euphorbia neriifolia* (L.) using response surface methodology. Microsc Res Tech. 2024;87(3):565–90. https://doi.org/10.1002/jemt.24456
8. Yadav P, Chaudhary P, Kumari D, Janmeda P. Assessment of phytochemical screening and antioxidant potential of *Heteropogon contortus* (L.) whole plant. Appl Biol Chem J. 2022;3(3):62–70. https://doi.org/10.52679/tabcj.2022.0007
9. Hayat K, Din IU, Alam K, et al. Green synthesis of zinc oxide nanoparticles using plant extracts of *Fumaria officinalis* and *Peganum harmala* and their antioxidant and antibacterial activities. Biomass Convers Biorefin. 2025;15:9565–79. https://doi.org/10.1007/s13399-024-05804-x
10. Shanmugam R, Tharani M, Abullais SS, et al. Black seed assisted synthesis, characterization, free radical scavenging, antimicrobial and anti-inflammatory activity of iron oxide nanoparticles. BMC Complement Med Ther. 2024;24:241. https://doi.org/10.1186/s12906-024-04552-9
11. Sasikumar JM, Salahadin A, Meseret CE, Jeyaramraja PR, Senthilkumar B. Biosynthesis of silver nanoparticles from *Verbena officinalis* L.: Characterization and antibacterial efficacy. Plant Sci Today. 2025;12(2):1–9. https://doi.org/10.14719/pst.5061
12. Pratap GP, Husain MK, Vallepu N, Gudivada S. Synthesis of silver nanoparticles using *Senna sophera* (L.) Roxb. leaf extract and study of antibacterial and anti-cancer properties. Plant Sci Today. 2024;11(4):1189–99. https://doi.org/10.14719/pst.3217
13. Kumari D, Singh D, Meena M, Janmeda P, Siddiqui MH. Qualitative, quantitative, *in vitro* antioxidant activity and chemical profiling of *Leptadenia pyrotechnica* (Forssk.) Decne using advanced analytical techniques. Antioxidants. 2024;13(7):794. https://doi.org/10.3390/antiox13070794
14. Fernandes RP, Trindade MA, Tonin FG, Lima CG, Pugine SM, Munekata PE, et al. Evaluation of antioxidant capacity of 13 plant extracts by three different methods. J Food Sci Technol. 2015;53:451–60. https://doi.org/10.1007/s13197-015-1994-x
15. Dinis TC, Madeira VM, Almeida LM. Action of phenolic derivatives as inhibitors of membrane lipid peroxidation and as peroxyl radical scavengers. Arch Biochem Biophys. 1994;315(1):161–69. https://doi.org/10.1006/abbi.1994.1485
16. Rathi K, Kumari D, Yadav P, Rawat V, Janmeda P, Verma VP. Synthesis, characterization and evaluation of antioxidant and antimicrobial activities of novel isatin derivatives. Arch Pharm. 2025;358:e70014. https://doi.org/10.1002/ardp.70014
17. Kurele RK, Rohit KS, Pawar G, Abdulah, Singh JP, Srinivasulu B. A comprehensive review on adulteration of raw materials used in ASU drug manufacturing. Int J Ayurveda Pharma Res. 2018;6(3):66–71.
18. Ansari SH. Essentials of Pharmacognosy. 1st ed. New Delhi: Birla Publications; 2006.
19. Laloo D, Kumar M, Prasad SK, Hemalatha S. Quality control standardization of the roots of *Potentilla fulgens* Wall.: A potent medicinal plant of the Western Himalayas and North-Eastern India. Pharmacogn J. 2013;5:97–103. https://doi.org/10.1016/j.phcgj.2013.04.002
20. Varshney N, Kumari D, Janmeda P, et al. *Salvadora oleoides* (Decne.): A systematic review and comprehensive botanical assessment. Discov Plants. 2025;2:140. https://doi.org/10.1007/s44372-025-00150-2
21. Sharma V, Janmeda P. Protective assessment of *Euphorbia neriifolia* and its isolated flavonoid against N-nitrosodiethylamine-induced hepatic carcinogenesis in male mice: A histopathological analysis. Toxicol Int. 2014;21(1):56–62. https://doi.org/10.4103/0971-6580.128790
22. Sharma V, Janmeda P. Curative effect of isolated flavonoid and *Euphorbia neriifolia* extract on hepatocarcinoma induced by N-nitrosodiethylamine in albino mice. Biochem Cell Arch. 2019;19(2):3205–11.
23. Jain D, Janmeda P. Ethnomedicinal, phytochemical and pharmacological investigations of *Gymnosporia senegalensis* Lam. Loes (Celastraceae). Proc Natl Acad Sci India B Biol Sci. 2025. https://doi.org/10.1007/s40011-025-01665-0
24. Pracheta, Sharma V, Paliwal R, Sharma S. *In vitro* free radical scavenging and antioxidant potential of ethanolic extract of *Euphorbia neriifolia* Linn. Int J Pharm Pharm Sci. 2011;3(1):238–42.
25. Jain D, Chaudhary P, Varshney N, Janmeda P. Carcinogenic effects of N-nitroso compounds in the environment. Environ Conserv J. 2020;21(3):25–41. https://doi.org/10.36953/ECJ.2020.21304

26. Kambale EK, Nkanga CI, Mutonkole BI, Bapolisi AM, Tassa DO, Liesse JMI, et al. Biosynthesis of antimicrobial silver nanoparticles using aqueous leaf extracts from three Congolese plant species. Heliyon. 2020;6:e04493. https://doi.org/10.1016/j.heliyon.2020.e04493

27. Bala N, Saha S, Chakraborty M, Maiti M, Das S, Basu R, et al. Biosynthesis of zinc oxide nanoparticles using *Hibiscus subdariffa* leaf extract. RSC Adv. 2015;5(7):4993–5003. https://doi.org/10.1039/C4RA12784F

28. Tettey C, Shin H. Evaluation of the antioxidant and cytotoxic activities of zinc oxide nanoparticles synthesized using *Scutellaria baicalensis* root. Sci Afr. 2019;6:e00157. https://doi.org/10.1016/j.sciaf.2019.e00157

29. Balogun SW, James OO, Sanusi YK, Olayinka OH. Biosynthesis and characterization of zinc oxide nanoparticles using *Mimosa pudica* leaf extract. SN Appl Sci. 2020;2:54. https://doi.org/10.1007/s42452-020-2127-3

30. Ansari MA, Jahan N. Structural and optical properties of BaO nanoparticles synthesized by facile co-precipitation method. Mater Highlights. 2021;2(1-2):23. https://doi.org/10.2991/mathi.k.210226.001

31. Devi HS, Singh TD. Iron oxide nanoparticles synthesis through a benign approach and its catalytic application. Perspect Sci. 2016;8:287–89. https://doi.org/10.1016/j.pisc.2016.04.054

32. Hussain A, Yasar M, Ahmad G, et al. Synthesis, characterization and applications of iron oxide nanoparticles. Int J Health Sci. 2023;17(4):3–10.

33. Ashrafi-Saiedlou S, Rasouli-Sadaghiani M, Fattahi M, et al. Biosynthesis and characterization of iron oxide nanoparticles fabricated using cell-free supernatant of *Pseudomonas fluorescens*. Sci Rep. 2025;15:1018. https://doi.org/10.1038/s41598-024-84974-0

34. Prasad C, Gangadhara S, Venkateswarlu P. Bio-inspired biosynthesis of Fe_3O_4 magnetic nanoparticles using watermelon rinds and their catalytic activity. Appl Nanosci. 2016;6(6):797–802. https://doi.org/10.1007/s13204-015-0485-8

35. Zambri NDS, Taib NI, Abdul Latif F, Mohamed Z. Utilization of neem leaf extract on biosynthesis of iron oxide nanoparticles. Molecules. 2019;24(20):3803. https://doi.org/10.3390/molecules24203803

36. Baabu PRS, Kumar HK, Gumpu MB, Babu KJ, Kulandaisamy AJ, Rayappan JBB. Iron oxide nanoparticles: A review on the province of its compounds, properties and biological applications. Materials (Basel). 2022;16(1):59. https://doi.org/10.3390/ma16010059

37. Lesiak B, Rangam N, Jiricek P, Gordeev I, Tóth J, Kövér L, et al. Surface study of Fe_3O_4 nanoparticles functionalized with biocompatible adsorbed molecules. Front Chem. 2019;7. https://doi.org/10.3389/fchem.2019.00642

38. Yassin MT, Al-Otibi FO, Al-Askar AA. Biosynthesis, characterization and antimicrobial activity of iron oxide nanoparticles with tigecycline against multidrug resistant bacterial strains. J King Saud Univ Sci. 2024;36(4):103131. https://doi.org/10.1016/j.jksus.2024.103131

39. Kumari D, Singh D, Meena M, et al. Phytocompounds and pharmacological insights of *Leptadenia pyrotechnica*: A new perspective on drug discovery. Discov Appl Sci. 2025;7:1089. https://doi.org/10.1007/s42452-025-07358-7

40. Amer MW, Awwad AM. Biosynthesis of copper nanoparticles by *Citrus limon* fruits extract: Characterization and antibacterial activity. Chem Int. 2021;7(1):1–8.

41. Lee J, Lee JH, Lee SY, et al. Antioxidant iron oxide nanoparticles: Their biocompatibility and bioactive properties. Int J Mol Sci. 2023;24(21):15901. https://doi.org/10.3390/ijms242115901

42. Duh PD. Antioxidant activity of burdock (*Arctium lappa* Linne): Its scavenging effect on free radical and active oxygen. J Am Oil Chem Soc. 1998;75:455–61. https://doi.org/10.1007/s11746-998-0248-8

43. Dinis TC, Madeira VM, Almeida LM. Action of phenolic derivatives as inhibitors of membrane lipid peroxidation and as peroxyl radical scavengers. Arch Biochem Biophys. 1994;315(1):161–69. https://doi.org/10.1006/abbi.1994.1485

44. Islam MF, Islam S, Miah MAS, Huq AO, Saha AK, Mou ZJ, et al. Biosynthesis of zinc oxide nanoparticles using *Allium cepa* L. waste peel extracts and its antioxidant and antibacterial activities. Heliyon. 2024;10(3):e25430. https://doi.org/10.1016/j.heliyon.2024.e25430

45. Abdelghany TM, Al-Rajhi AM, Yahya R, Bakri MM, Al Abboud MA, Qanash H, et al. Phyto-fabrication of zinc oxide nanoparticles with advanced characterization and its antioxidant, anticancer and antimicrobial activity. Biomass Convers Biorefin. 2023;13(1):417–30. https://doi.org/10.1007/s13399-022-03412-1

46. Grudlewska-Buda K, et al. Antibiotic resistance in selected emerging bacterial foodborne pathogens-An issue of concern? Antibiotics. 2023;12:880. https://doi.org/10.3390/antibiotics12050880

47. Liang T, et al. Simultaneous detection of viable *Salmonella* spp., *Escherichia coli* and *Staphylococcus aureus* using PMA with multiplex real-time quantitative PCR. Food Sci Nutr. 2022;10:3165–74. https://doi.org/10.1002/fsn3.2916

48. Shashiraj KN, et al. Exploring the antimicrobial, anticancer and apoptosis-inducing ability of biofabricated silver nanoparticles using *Lagerstroemia speciosa*. Bioengineering. 2023;10:821. https://doi.org/10.3390/bioengineering10070821

49. Khaleel DS, Mutter TY, Huang X. Potential mechanism of gallic acid-coated iron oxide nanoparticles against genes of *Klebsiella pneumoniae* capsule. Microsc Res Tech. 2024;87(11):2774–84. https://doi.org/10.1002/jemt.24650

50. Kakian F, Mirzaei E, Moattari A, et al. Determining the cytotoxicity of the minimum inhibitory concentration of silver and zinc oxide nanoparticles in ESBL and carbapenemase producing *Proteus mirabilis* isolated from clinical samples in Shiraz, Southwest Iran. BMC Research Notes. 2024;17(1):40. https://doi.org/10.1186/s13104-023-06402-2

Additional information

Peer review: Publisher thanks Sectional Editor and the other anonymous reviewers for their contribution to the peer review of this work.

Reprints & permissions information is available at https://horizonepublishing.com/journals/index.php/PST/open_access_policy

Publisher's Note: Horizon e-Publishing Group remains neutral with regard to jurisdictional claims in published maps and institutional affiliations.

Indexing: Plant Science Today, published by Horizon e-Publishing Group, is covered by Scopus, Web of Science, BIOSIS Previews, Clarivate Analytics, NAAS, UGC Care, etc
See https://horizonepublishing.com/journals/index.php/PST/indexing_abstracting

Copyright: © The Author(s). This is an open-access article distributed under the terms of the Creative Commons Attribution License, which permits unrestricted use, distribution and reproduction in any medium, provided the original author and source are credited (https://creativecommons.org/licenses/by/4.0/)

Publisher information: Plant Science Today is published by HORIZON e-Publishing Group with support from Empirion Publishers Private Limited, Thiruvananthapuram, India.